Available online at https://link.springer.com/journal/42241
http://www.jhydrodynamics.com
Journal of Hydrodynamics, 2020, 32(6): 1122-1137
https://doi.org/10.1007/s42241-020-0080-7

The effects of caudal fin deformation on the hydrodynamics of thunniform swimming under self-propulsion *

Yi-kun Feng[1], Yu-min Su[1], Huan-xing Liu[2], Yuan-yuan Su[3]
1. *College of Shipbuilding Engineering, Harbin Engineering University, Harbin 150001, China*
2. *Beijing Institute of Specialized Machinery, Beijing 100081, China*
3. *Science College, Harbin Engineering University, Harbin 150001, China*

(Received August 10, 2019, Revised April 22, 2020, Accepted April 30, 2020, Published online December 28, 2020)

Abstract: To investigate the effects of the caudal fin deformation on the hydrodynamic performance of the self-propelled thunniform swimming, we perform fluid-body interaction simulations for a tuna-like swimmer with thunniform kinematics. The 3-D vortices are visualized to reveal the role of the leading-edge vortex (LEV) in the thrust generation. By comparing the swimming velocity of the swimmer with different caudal fin flexure amplitudes f_a, it is shown that the acceleration in the starting stage of the swimmer increases with the increase of f_a, but its cruising velocity decreases. The results indicate that the caudal fin deformation is beneficial to the fast start but not to the fast cruising of the swimmer. During the entire swimming process, the undulation amplitudes of the lateral velocity and the yawing angular velocity decrease as f_a increases. It is found that the formation of an attached LEV on the caudal fin is responsible for generating the low-pressure region on the surface of the caudal fin, which contributes to the thrust. Furthermore, the caudal fin deformation can delay the LEV shedding from the caudal fin, extending the duration of the low pressure on the caudal fin, which will cause the caudal fin to generate a drag-type force over a time period in one swimming cycle and reduce the cruising speed of the swimmer.

Key words: Computational fluid dynamics (CFD) numerical simulation, self-propulsion, caudal fin, deformation

Introduction

In nature, fish can have complex and diverse movements with various fins on their body, such as the fast-start, the periodic cruising, the steering and the hovering. The excellent swimming performances of fish have attracted many researches during the last hundreds of years. The swimming modes of fish are generally divided into two categories: the body and caudal fin (BCF) mode and the median and pair fins (MPFs) mode[1]. The BCF propulsion has five different types: the anguilliform, the sub-carangiform, the carangiform, the thunniform and the ostraciform[2]. Only approximately 12% of fish families use the MPF mode as their routine propulsive mode[3].

In this paper, we focus on the thunniform mode of swimming. For a thunniform swimmer, a significant lateral undulation occurs at the posterior 1/3 of the body and the maximum amplitude is reached at the end of the tail peduncle[4]. As the primary swimming mode for many fast fish, the thunniform mode of swimming has attracted a constant attention of scientists. Numerous experimental studies of live fish, focused on the flow field characteristics of the anguilliform, carangiform and thunniform swimmers with the help of the particle image velocimetry (PIV) technology. A double vortex row was observed in anguilliform swimmers[5], in which the wake structure contains two disconnected vortex rings, while in the carangiform and thunniform swimmers one sees a single vortex row with a series of connected vortex rings in the flow field[6]. However, the parameterization experiments based on live fish are either difficult or unfeasible, as it is difficult not only to control the swimming of fish, but also to obtain the transient distribution of the surface pressure of fish[7]. Therefore, a large number of numerical simulations were conducted for the fish swimming. Numerical simulations of fish swimming can be

* Project supported by the National Natural Science Foundation of China (Grant No. 51479039).
Biography: Yi-kun Feng (1992-), Male, Ph. D. Candidate,
E-mail: fykbionic@163.com
Corresponding author: Yu-min Su,
E-mail: suyumin@hrbeu.edu.cn

divided into three types: the steady swimming of fish immersed in a uniform incoming flow[6, 8-9], the forward swimming of fish with one degree of freedom (1DOF)[10] and the free swimming of fish with three degrees of freedom (3DOF)[11-14]. For the steady swimming, Liu et al.[9] conducted numerical studies of the vortex structures and the hydrodynamic performances of the fish body with interactions between the flexible dorsal, and anal and caudal fins. For the 1DOF forward swimming of fish, Borazjani and Daghooghi[10] simulated the attachment of the leading-edge vortex (LEV), generated by different tails of a mackerel with carangiform kinematics. For the 3DOF self-propelled fish swimming, Kern and Koumoutsakos[11] investigated the hydrodynamics of the anguilliform swimming.

These experimentalal and numerical studies focused on the characteristics of the trailing wake generated by the fish, but without paying enough attention to the features of the LEV of fish, especially the characteristics of the LEV generated by the flexible caudal fin of fish. In this paper we investigate the different effects of rigid and flexible caudal fins on the mechanism of hydrodynamics and 3-D wake structures for self-propelled thunniform swimming, with numerical simulations of a self-propelled tuna-l ike fish body with different caudal fin flexibilities to understand the fundamental physical mechanisms of the hydrodynamic role of the caudal fin's flexibility and the role of the LEV in the contribution of the pressure distribution on the caudal fin and the force it generates.

1. Materials and methods

1.1 *Computation model and kinematics*

In this work, the swimmer has the same geometric profile as the "Fangsheng-I", a laboratory robot that imitates the body shape and the motion of a tuna[15]. The total length L of the swimmer (from head to caudal fin) is 2.40 m, and the maximal width B_m of the swimmer (with the pectoral fins) is 1.16 m. The swimmer has a crescent-shaped caudal fin of NACA0018 shaped cross sections. The chord length C of the caudal fin is 0.31 m, which is defined as the linear distance between the leading edge point and the line segment between two caudal fin tips. The live tunas, the"FangSheng-I" bionic robotic fish and the virtual swimmer are shown in Fig. 1. In this work, the swimmer swims freely in the X-Y plane of the global frame, and the prescribed undulation motion of the swimmer body is made in the body-fixed frame.

For the thunniform swimming, the front 2/3 of the swimmer body is too stiff to have undulation and deformation, and the significant lateral movements are observed only at the caudal fin[16]. Therefore, the

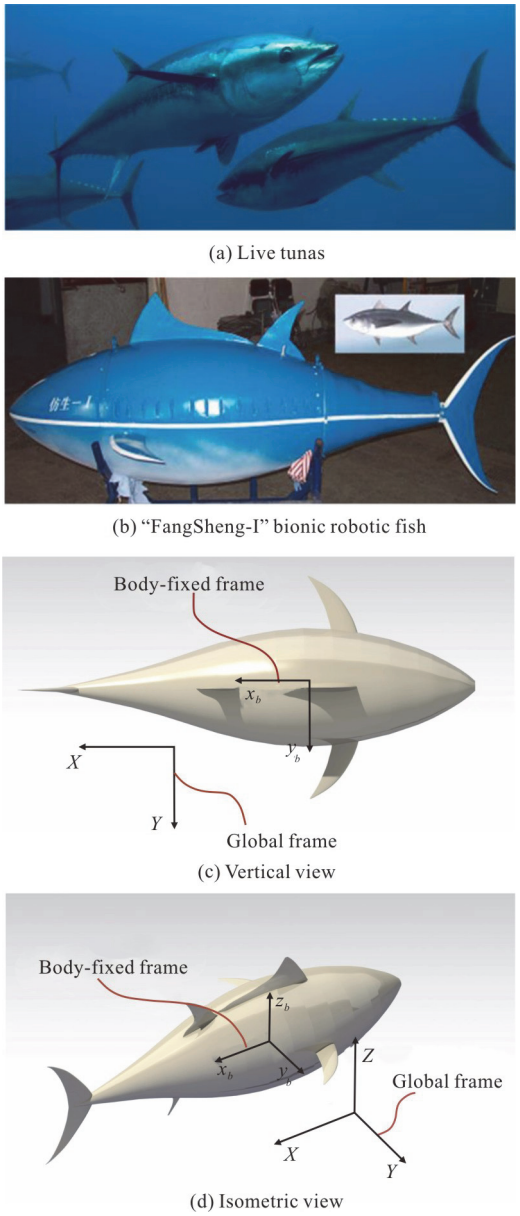

Fig. 1 (Color online) Computational model and two coordinate systems

swimmer body can be divided into three parts: the rigid front body, the flexible rear body and the caudal fin, as shown in Fig. 2. Then, the prescribed kinematics of the swimmer can be divided into two parts: the lateral undulation of the flexible rear body and the heaving-pitching motion of the caudal fin[4]. First, the lateral undulation of the flexible rear body is characterized by a backward traveling wave[4], described as

$$y(x,t) = a(x)\sin(2\pi ft - kx) \tag{1}$$

where $y(x,t)$ is the lateral displacement of the mid-line, x is the axial position, t is the time, f is the

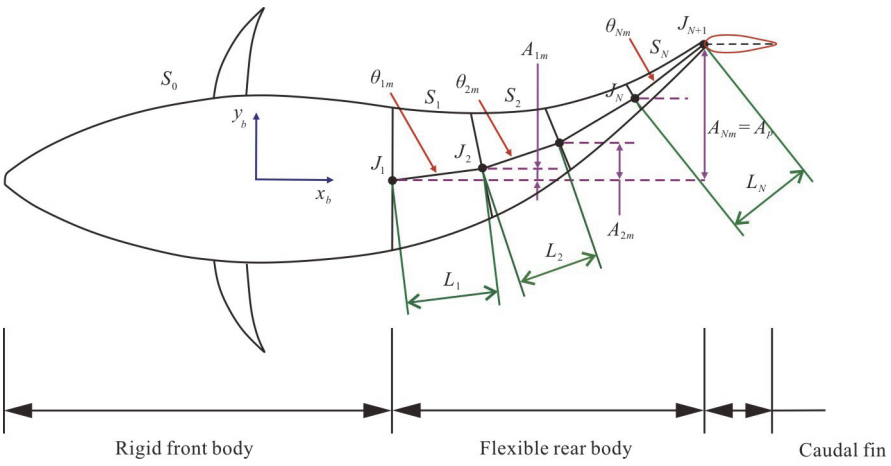

Fig. 2 (Color online) Multi-joint undulation motion of the swimmer

undulating frequency, k is the wave number, and the amplitude envelope $a(x)$ of the lateral undulation is approximated with a quadratic function[4, 8], as denoted in this work as $a(x)$, a quadratic polynomial[4]

$$a(x) = A_p\left(\frac{x-x_f}{L_f}\right)^2 \tag{2}$$

where A_p is the lateral undulation amplitude of the tail peduncle joint, x_f is the beginning of the flexible rear body and L_f is the length of the flexible rear body.

In this work, to conform with the previous experimental investigation of the "Fangsheng-I"[15] and the other numerical simulations[4, 17] in our laboratory, k is set at zero. In addition, the value of our defined k is more conducive to the heaving-pitching motion of the caudal fin, which also makes it convenient to systematically study the effect of the motion parameters of the caudal fin on the hydrodynamic performance of the entire fish. The effect of k on the swimming will be discussed in our future papers.

If we directly use Eq. (1) to define the lateral undulation of the flexible rear body, the body will be elongated during swimming. To address this problem, Li et al.[12] introduced a correction factor in Eq. (1) to ensure that the length of the swimmer remains unchanged. In view of the multi-joint vertebrae of live fish, the flexible rear body is divided into enough segments to emulate the undulation motion and ensure that the body length is unchanged by keeping the length of every segment unchanged during the undulation motion.

In Fig. 2, the rigid front body of the swimmer is denoted by S_0. The flexible rear body is divided into N segments, denoted by $S_i\,(i=1,2,\cdots,N)$, the length of each segment is L_i. The rotation joint of each segment S_i is denoted by J_i with the coordinates $(J_{ix}(t), J_{iy}(t))$ under the body-fixed frame. The coordinate of the first rotation joint J_1 is $(x_f, 0)$. The rotation joint of the caudal fin is denoted by $J_{N+1}\,(J_{(N+1)x}(t), J_{(N+1)y}(t))$. Thus, the motion of each segment S_i can be decomposed into the translation motion with J_i and the rotation motion around J_i. The caudal fin undergoes a translation motion with J_{N+1} and a pitch motion around J_{N+1}.

During the undulation motion of the flexible rear body, the amplitude of the translation motion of each segment is denoted by $A_{im}\,(i=1,2,\cdots,N)$. Then we can determine A_{im} from Eqs. (1), (2) as follows:

$$A_{im} = A_p\left(\frac{\sum_{t=1}^{i} L_t}{L_f}\right)^2,\quad i=1,2,\cdots,N,\quad A_{Nm}=A_p \tag{3}$$

The amplitude of the rotation motion of each S_i around J_i is denoted by $\theta_{im}\,(i=1,2,\cdots,N)$, which can be expressed as:

$$\theta_{1m} = \arcsin\left(\frac{A_{1m}}{L_1}\right),\quad \theta_{im} = \arcsin\left(\frac{A_{im}-A_{(i-1)m}}{L_i}\right),$$

$$i = 2,3,\cdots,N \tag{4}$$

Then we use Eq. (4) to determine the rotation motion of each segment S_i around J_i, which can be expressed as:

$$\theta_i(t) = \theta_{im}\sin(2\pi ft),\ i = 1, 2, \cdots, N \tag{5}$$

Based on Eq. (5), we can obtain $J_{ix}(t)$, $J_{iy}(t)$, $J_{(N+1)x}(t)$ and $J_{(N+1)y}(t)$ in the following form:

$$J_{1x}(t) = x_f,\ J_{1y}(t) = 0,$$

$$J_{ix}(t) = J_{(i-1)x}(t) + L_{(i-1)}\cos[\theta_{i-1}(t)],$$

$$J_{iy}(t) = J_{(i-1)y}(t) + L_{(i-1)}\sin[\theta_{i-1}(t)],$$

$$i = 2, 3, \cdots, N,\ J_{(N+1)x}(t) = J_{Nx}(t) + L_N\cos[\theta_N(t)],$$

$$J_{(N+1)y}(t) = J_{Ny}(t) + L_N\sin[\theta_N(t)] \tag{6}$$

The caudal fin motion frequency is equal to that of the flexible body's undulation motion, and the translation motion and the pitch motion have a phase angle φ, which is set to a value of 90°[4, 18]. We then have the kinematics of the caudal fin as follows:

$$x_f(t) = x_f + \sum_{i=2}^{N} L_i\cos\{\arcsin\{[A_p(\sum_{t=1}^{i} L_t\cdot L_f^{-1})^2 -$$

$$A_p(\sum_{i=2}^{n-1} l_i\cdot L_f^{-1})^2]L_i^{-1}\}\sin(2\pi ft)\} +$$

$$L_1\cos\{\arcsin\{[A_p(L_1\cdot L_f^{-1})^2 L_1^{-1}\}\sin(2\pi ft)\},$$

$$y_f(t) = \sum_{i=2}^{N} L_i\sin\{\arcsin\{[A_p(\sum_{t=1}^{i} L_t\cdot L_f^{-1})^2 -$$

$$A_p(\sum_{t=1}^{i-1} L_t\cdot L_f^{-1})^2]L_i^{-1}\}\sin(2\pi ft)\} +$$

$$L_1\sin\{\arcsin\{[A_p(L_1\cdot L_f^{-1})^2]L_1^{-1}\sin(2\pi ft)\} \tag{7}$$

$$\theta_f(t) = \theta_{\mathrm{fm}}\sin(2\pi ft - \varphi) \tag{8}$$

where $x_f(t)$, $y_f(t)$ denote the translation motion of the caudal fin in the x_b-, y_b-directions, respectively, and θ_{fm} is the pitch motion amplitude.

For the deformation of the caudal fin, only the deformation in the chordwise direction is considered. The deformation profile is determined with an analysis of the effect of the flexure amplitude, described as[18]

$$y_{ca}(x_{ca}, t) = -\frac{f_a}{C}(x_{ca} - x_{ca0})^2\sin(2\pi ft - \psi) \tag{9}$$

where f_a is the flexure amplitude, x_{ca0} is the x_b-coordinate of the starting point of the deformation and ψ is the phase angle of the deformation, which is set to 90°. In our study, f_a is taken as 0, 0.1,···, 0.5, when f_a is 0, the caudal fin is rigid and not deformed.

1.2 *Numerical method*

In this work, a 3DOF fluid-body interaction numerical simulation scheme is employed to study the effect of the caudal fin deformation on the self-propelled swimming. The flow field is simulated using the commercial CFD solver package FLUENT. The FLUENT was successfully used to simulate fish's self-propelled swimming[19], and the accuracy of the solver was validated extensively for flows with various bionic swimming[4, 18, 20]. The related validations of this solver can be found in our previous publications[4, 18-19]. The governing equations are 3-D viscous incompressible Navier-Stokes equations in a body-fixed coordinate system that is translating with a linear velocity $\boldsymbol{u}_c$ and rotating with an angular velocity $\boldsymbol{\omega}$ relative to the global coordinate system[21]:

$$\nabla\cdot\boldsymbol{u}_r = 0 \tag{10}$$

$$\frac{\partial\boldsymbol{u}}{\partial t} + \nabla\cdot(\boldsymbol{u}_r\boldsymbol{u}) + \boldsymbol{\omega}\times(\boldsymbol{u} - \boldsymbol{u}_c) = -\frac{1}{\rho}\nabla p + \frac{\mu}{\rho}\nabla^2\boldsymbol{u} \tag{11}$$

where $\boldsymbol{u}$ is the absolute velocity (the velocity viewed from the global coordinate system), $\boldsymbol{u}_r$ is the relative velocity (the velocity viewed from the body-fixed coordinate system), ρ is the fluid density, p is the pressure and μ is the dynamic viscosity.

The governing equations Eqs. (10), (11) are discretized using the finite volume method with the pressure-based transient solver. The SIMPLE algorithm is applied for the pressure-velocity coupling, with a first-order implicit discretization in time and a second-order upwind in space. To deal with the flow in a domain with complex 3-D flexible fish moving in prescribed kinematics, the no-slip boundary condition is imposed on the moving boundary:

$$\boldsymbol{u}=\boldsymbol{u}_s \tag{12}$$

where $\boldsymbol{u}_s$ is the velocity of the swimmer's surface.

The velocity of a flexible body can be decomposed into a rigid whole-body motion and a deformation motion[22]

$$\boldsymbol{u}_s=\boldsymbol{u}_c+\boldsymbol{\omega}\times\boldsymbol{r}+\boldsymbol{u}_{def}\ \ \boldsymbol{u}_s=\boldsymbol{u}_c+\boldsymbol{\omega}\times\boldsymbol{r}+\boldsymbol{u}_{\mathrm{def}} \tag{13}$$

where $\boldsymbol{r}$ is the position vector from the COM, and is the specified velocity of the deforming motion presented in Section 1.1 in the body-fixed coordinate system.

In the current 3DOF self-propelled swimming, the whole-body motion of the swimmer is computed using the Newton's motion (momentum) equations:

$$m\frac{\mathrm{d}U_{cX}}{\mathrm{d}t}=F_X,\ \ m\frac{\mathrm{d}U_{cY}}{\mathrm{d}t}=F_Y,$$

$$\frac{\mathrm{d}(\omega_z I_z)}{\mathrm{d}t}=I_z\frac{\mathrm{d}\omega_z}{\mathrm{d}t}+\omega_z\frac{\mathrm{d}I_z}{\mathrm{d}t}=M_z \tag{14}$$

where m is the swimmer's mass, U_{cX}, U_{cY} are the components of the translation velocity $\boldsymbol{u}_c$ in X, Y directions, respectively, F_X, F_Y are the components of the hydrodynamic force in X, Y directions, respectively, I_z is the inertial moment about the yawing axis through the COM, ω_z is the yawing angular velocity and M_z is the yaw moment. The effect of the inertial and external forces and moments on the swimmer that are independent of the fluid motion, such as the gravitational force, are not considered in this work, similar to other published studies of self-propelled swimming[11-12, 19].

During the simulation, F_X and F_Y can be computed by an integral of the local pressure and the viscous forces acting on the swimmer surface[8].

$$\boldsymbol{F}=F_X=\int_S(-\boldsymbol{p}\boldsymbol{n}_1+\boldsymbol{\tau}_{1j}\boldsymbol{n}_j)\,\mathrm{d}S,$$

$$\boldsymbol{F}=F_Y=\int_S(-\boldsymbol{p}\boldsymbol{n}_2+\boldsymbol{\tau}_{2j}\boldsymbol{n}_j)\,\mathrm{d}S \tag{15}$$

where $\boldsymbol{p}$ is the pressure vector on $\mathrm{d}S$, $\boldsymbol{n}_j$ is the jth component of the unit normal vector on $\mathrm{d}S$ and $\boldsymbol{\tau}_{ij}$ is the viscous stress tensor on $\mathrm{d}S$. The yaw moment M_z with respect to the swimmer's COM can be calculated as

$$M_z=\int_S\{\boldsymbol{r}\times[(-\boldsymbol{p}\boldsymbol{n}_1+\boldsymbol{\tau}_{1j}\boldsymbol{n}_j)\boldsymbol{n}_1+(-\boldsymbol{p}\boldsymbol{n}_2+\boldsymbol{\tau}_{2j}\boldsymbol{n}_j)\boldsymbol{n}_2]\}\mathrm{d}S \tag{16}$$

In this work, the swimmer swims in the negative X direction. Therefore, when F_X is in the positive X direction (with a positive value), it is considered as the drag type, when F_X is in the negative X direction (with a negative value), it is considered as the thrust type. However, whether F_X is the drag type or the thrust type, it consists of a pure thrust T_{pur} and a pure resistance R_{pur}. In order to separate these two forces, we use the method proposed by Borazjani and Sotiropoulos[8].

$$T_{\mathrm{pur}}=-\frac{1}{2}[(\int_S-\boldsymbol{p}\boldsymbol{n}_1\,\mathrm{d}S-\left|\int_S-\boldsymbol{p}\boldsymbol{n}_1\,\mathrm{d}S\right|)+$$

$$(\int_S\boldsymbol{\tau}_{1j}\boldsymbol{n}_{1j}\,\mathrm{d}S-\left|\int_S\boldsymbol{\tau}_{1j}\boldsymbol{n}_{1j}\,\mathrm{d}S\right|)] \tag{17}$$

$$R_{\mathrm{pur}}=\frac{1}{2}[(\int_S-\boldsymbol{p}\boldsymbol{n}_1\,\mathrm{d}S+\left|\int_S-\boldsymbol{p}\boldsymbol{n}_1\,\mathrm{d}S\right|)+$$

$$(\int_S\boldsymbol{\tau}_{1j}\boldsymbol{n}_{1j}\,\mathrm{d}S+\left|\int_S\boldsymbol{\tau}_{1j}\boldsymbol{n}_{1j}\,\mathrm{d}S\right|)] \tag{18}$$

The instantaneous power consumption P_{hydro} due to the undulation of the swimmer body is calculated as follows[8]

$$P_{\mathrm{hydro}}=[\int_S(-\boldsymbol{p}\boldsymbol{n}_i\,\dot{y}_i)\,\mathrm{d}S+\int_S(\boldsymbol{\tau}_{ij}\boldsymbol{n}_j\,\dot{y}_i)\,\mathrm{d}S] \tag{19}$$

where $\dot{y}_i$ is the time derivative of the displacement of the swimmer surface, i.e., the velocity of the undulations of the swimmer, in the ith direction.

Then, in order to evaluate the influence of the caudal fin deformation on the swimming efficiency of the swimmer, the Froude efficiency η_f proposed by Tytell[5] is adopted

$$\eta_f=\frac{\overline{T}_{\mathrm{pur}}U}{\overline{T}_{\mathrm{pur}}U+\overline{P}_{\mathrm{hydro}}} \tag{20}$$

where $\overline{T}_{\mathrm{pur}}$ is the cycle-averaged value of the thrust force, U is the cycle-averaged value of the forward velocity and $\overline{P}_{\mathrm{hydro}}$ is the cycle-averaged value of the power consumption.

In this work, the computational domain is an

$8.5L(X)\times 2.0L(Y)\times 1.0L(Z)$ cubic tank, which is discretized with a grid including 3.57×10^6 elements. The domain size is tested to be sufficiently large that the influence of the boundary can be ignored. The boundary conditions of the computational domain are set as follows: (1) zero velocity and zero gradient of the pressure on the inlet and far-field boundaries, (2) zero gradient of both the velocity and the pressure on the outlet boundary. The computational domain is divided into three domains: the outer domain (denoted by D1) and two inner domains (denoted by D2 and D3), as illustrated in Fig. 3(a). The swimmer is placed in D2 and D3, specifically, the rigid front body is placed in D2 and the flexible rear body and the caudal fin are placed in D3. The swimmer surface is discretized with triangular elements, and the meshes are sufficiently refined in the regions with a large curvature to ensure the capture of the geometry of the swimmer body and to ensure that the boundary layer is well processed when generating the 3-D meshes. A uniform mesh with constant spacing of $1/60L$ is used on the interfaces between the inner and outer domains. D2 and D3 are discretized with unstructured tetrahedron meshes, which are locally refined near the surfaces of the swimmer with an element spacing size of $0.0005L$ to keep the y^+ values on the swimmer surface from 30 to 150 during the entire swimming process, similar to the approach used by Li et al.[19]. The SST k-ω model is applied for the effect of the turbulence, which was fully validated by Leroyer and Visonneau[23] in the simulation of fish's self-propelled swimming. The mesh size and the growth rate from the surfaces of the swimmer to the boundaries of the inner domains are properly controlled to ensure the quality of the meshes. In D1, the meshes are unstructured in the regions adjacent to D2 and D3, and the other regions are discretized with hexahedral meshes. In addition, the mesh is rapidly stretched in the directions of the swimmer height and width. In the longitudinal direction, the grid stretching is rapid in the upstream region of the swimmer, while in the near wake region the stretching ratio of the mesh is kept below 2% (approximately equal to 1.7%) so as to keep a relatively high streamwise resolution. A combination of smoothing and remeshing is used to regenerate and smooth the meshes inside D2 and D3 after each time-step. The parameters of the smoothing and remeshing approaches are selected reasonably to ensure the quality of meshes.

It can be seen from Fig. 3(a) that with this mesh division strategy, we can well deal with both the undulation motion of the flexible rear body and the flexible deformation of the caudal fin. The flexible deformation of the caudal fin during a quarter cycle is illustrated in Fig. 3(b), where the arrow points to the flexible deformation direction of the caudal fin.

2. Results and discussions

U_{cx} and U_{cy} are the longitudinal velocity and the lateral velocity of the swimmer, respectively, and F_x and F_y are the longitudinal force and the lateral force of the swimmer, respectively. During the simulation, the swimmer is accelerated from rest with $U_{cx}=0$, $U_{cy}=0$ and $\omega_z=0$ to the cruising state with an asymptotic mean value of U_{cx} and a zero mean value of U_{cy} and ω_z. Because the swimmer is swimming in the negative x_b-direction, for convenience of analyzing, the forward velocity U_f is set to be equal to the negative of U_{cx} and the longitudinal net force F_l to be equal to the negative of F_x. When the swimmer reaches the cruising state, the cycle-averaged value of U_f is set to be equal to U_{cf}, which is called the cruising velocity. As reported

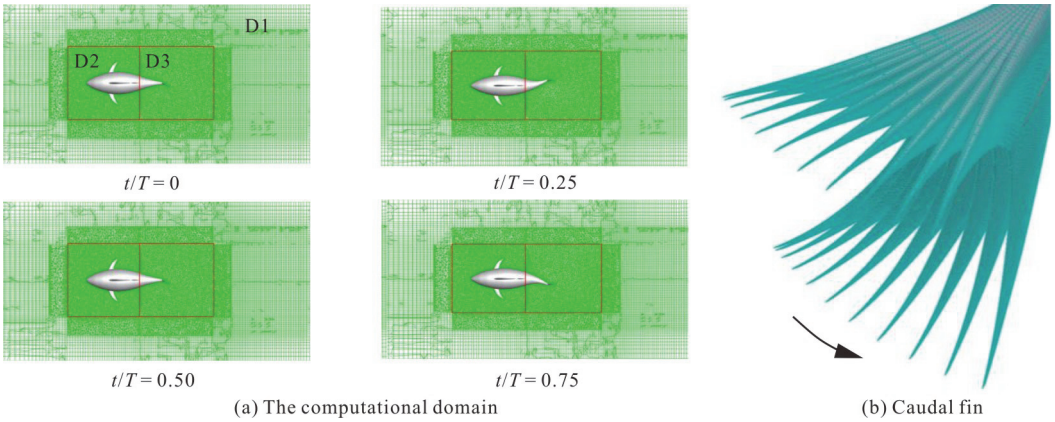

Fig. 3 (Color online) Computational mesh

in the experiment by Donley and Dickson[24], the lateral undulation amplitude A_p of the tail peduncle joint ranges from $0.052L$ to $0.082L$. In this section, we conduct a parametric study of the effect of the flexure amplitude F_a of the caudal fin on the swimmer's self-propelled swimming. The value of A_p is set as $0.5C$ $(0.065L)$, within the range reported by Donley and Dickson[24]. The other parameters are set as $\theta_{fm} = 25°$, $f = 1.0$ Hz. Then, the Reynolds number $Re = \rho U_{cf} L / \mu$, and the Strouhal number $St = 2A_p f / U_{cf}$, the two non-dimensional parameters that characterize the swimming performance of the fish's self-propelled swimming, can be obtained.

2.1 *Sensitivity study and validation*

2.1.1 Sensitivity study

The mesh dependence test is conducted using three meshes with 2.54 (coarse), 3.57 (medium) and 6.79 (fine) million elements. Figure 4(a) shows the time history of U_f for different grids with a time-step size $\Delta t = T/200$. It can be seen that the values of U_f calculated by the medium and fine grids are very close (the calculated value of U_{cf} of the fine grid is 0.78% larger than that of the medium grid), while the result of the coarse grid is not good. Therefore, we choose the medium grid in all simulations. A sensitivity study of the time-step is also conducted, with $\Delta t = \{T/400, T/200, T/100\}$ using the medium grid. Figure 4(b) shows the time history of U_{cf} obtained with different time-steps using the medium gird. It can be seen that with both $\Delta t = T/400$, $\Delta t = T/200$, reasonable results are obtained and the calculated values of U_{cf} are in good agreement (the calculated value of U_{cf} is 0.5% larger at $\Delta t = T/200$ than that at $\Delta t = T/400$), while with $\Delta t = T/100$ the result is not good. Hence, the medium grid and $\Delta t = T/200$ are selected in all simulations in this work and the CPU time of one swimming cycle is about 4.5 h in a PC with Intel Core i9-7900x processor and 64 Gigabytes of memory.

2.1.2 Validation

Based on our previous experiments on "FangSheng-I"[15] and our numerical simulation only with 1DOF in the forward direction[17], we validate the ability of the fluid-body interaction method to deal with the fish's 3DOF self-propelled swimming. $A_p = 0.3C$, $f_a = 0$ and $\theta_{fm} = 25°$ are unchanged throughout the experiment, where the cruising velocity U_{cf} of "FangSheng-I" for various values of f is obtained. The comparison results are shown in Fig. 5 and the solid lines in the figure are quadratic fitting curves. From Fig. 5 we can see that our current calculation results are better than those of Zhang[17]. It can also be seen that the results obtained by our current method are in the same overall trends as the experimental results, whereas the trend obtained by Zhang[17] is quite different from the trend of the experimental results. The reason for this is that Zhang[17] used the 1DOF numerical method while this paper use the 3DOF numerical method.

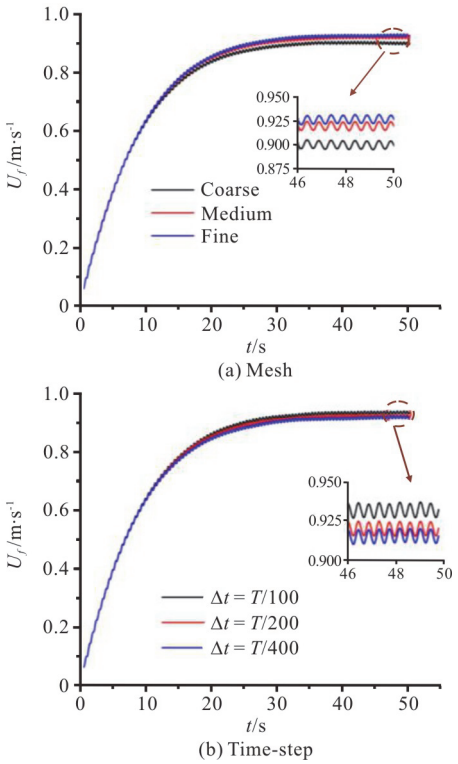

Fig. 4 (Color online) Sensitivity study

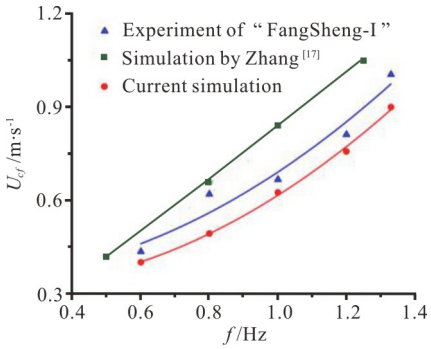

Fig. 5 (Color online) Comparison of computed cruising velocity with previous experimental and numerical results for different values of f

The implementation of the fluid-body coupling framework is also validated by the test case of an anguilliform fish undergoes a self-propelled swimming. The length of the fish body is $L = 1\,\mathrm{m}$. In this validation, we use the mesh generation scheme presented in Section 1.2 to generate the numerical grid and the numerical approach presented in Section 1.2 to simulate the flow. The fish geometry is taken from Kern and Koumoutsakos[11]. More details about the fish geometry and the calculation parameters can be found in Kern and Koumoutsakos[11]. The geometry of the resulting 3-D deformed body during the undulation is illustrated in Fig. 6(a). The undulation of the fish is described by the lateral deformation $y(s,t)$ of the midline s of the body, described as

$$y(s,t) = 0.125\frac{s + 0.03125}{1.03125}\sin\left[2\pi\left(s - \frac{t}{T}\right)\right] \tag{21}$$

Figure 6(b) shows the time history of the forward velocity U_f of the anguilliform fish. The fish reaches a cruising velocity of $U_{cf} = 0.381\,\mathrm{L/s}$, which matches well with the numerical results reported by Kern and Koumoutsakos[11] where the cruising velocity is 0.400 L/s.

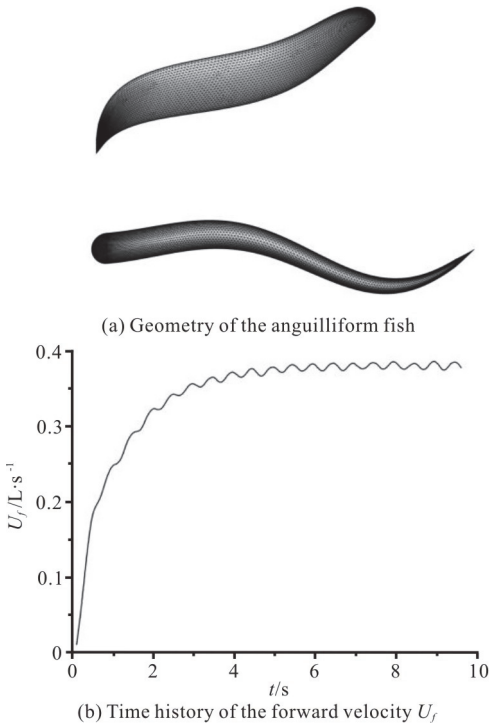

Fig. 6 Validation of a self-propelled anguilliform fish

2.2 *Swimming performance*

The time history of the forward velocity U_f for different f_a is illustrated in Fig. 7. It can be observed that the cruising velocity U_{cf} and the time t_{cf} for the swimmer to reach the cruising state decrease with the increase of f_a, as can clearly be seen in Table 1, and Re is in the range of 1.86×10^6-2.20×10^6. With the increase of f_a, the acceleration of the swimmer's starting motion increases, that is, the flexible deformation of the caudal fin can provide a larger burst force for the swimmer to start, which becomes larger with the increase of f_a. During the cruising state, the U_f slightly fluctuates around the U_{cf}, as shown in the insets in Fig. 7, where the fluctuations of the U_f are approximately 0.51%, 0.47%, 0.47%, 0.57%, 0.72% and 1.11% for their respective U_{cf} values when f_a varies from 0 to 0.5.

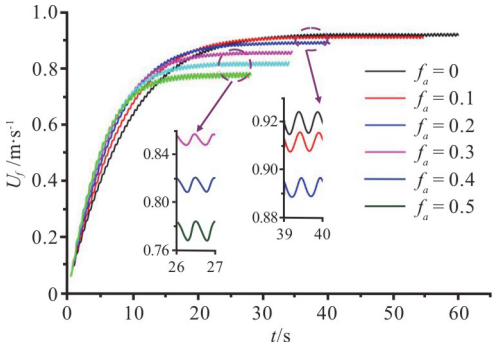

Fig. 7 (Color online) Time history of the forward velocity U_f for different f_a

Table 1 Cruising velocity and time for each swimmer to reach the cruising state

f_a	U_{cf} /m·s^{-1}	t_{cf} /s
0	0.920	42
0.1	0.912	40
0.2	0.892	36
0.3	0.856	30
0.4	0.817	26
0.5	0.777	24

During the self-propelled swimming, the time variations of the lateral velocity U_{cy} and the yawing angular velocity ω_z for different f_a are shown in Figs. 8(a), 9(a), respectively. Figures 8(b) and 9(b) show the time variations of U_{cy}, ω_z in one swimming period during the cruising state, respectively. From Figs. 8, 9, we can see that during the entire swimming process, the fluctuation amplitudes of U_{cy}, ω_z of a swimmer with a larger f_a are always smaller than those of a swimmer with smaller

f_a. These characteristics of U_{cy}, ω_z indicate that the flexible deformation of the caudal fin is conducive to the forward direction stability of the swimmer's self-propelled swimming.

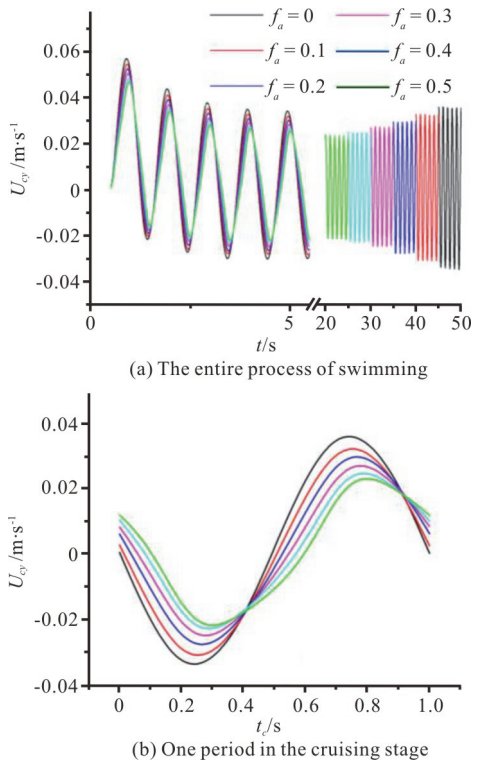

(a) The entire process of swimming

(b) One period in the cruising stage

Fig. 8 (Color online) Time history of lateral velocity U_{cy} for different f_a

2.3 *Hydrodynamic performance and swimming efficiency*

The longitudinal net forces of the whole swimmer body, the rigid front body, the flexible rear body and the caudal fin are denoted by F_l, F_{lrf}, F_{lfr} and F_{lcf}, respectively. In order to explore the reasons for the differences in the swimming performance of the swimmer with different f_a, Fig. 10 shows the cycle-averaged values of F_l, F_{lrf}, F_{lfr} and F_{lcf} for the swimmer with different f_a. It can be observed from Fig. 10(a) that in all cases, the cycle-averaged value of F_l decreases monotonically from a positive value to zero, this trend leads to a gradual increase of U_f from zero to a constant value (Fig. 7). At the beginning of the swimming, the cycle-averaged value of F_l becomes larger with the increase of f_a, which leads to a faster increase of U_f in the larger f_a case. However, the larger the f_a, the faster the decrease of the cycle-averaged value of F_l, which

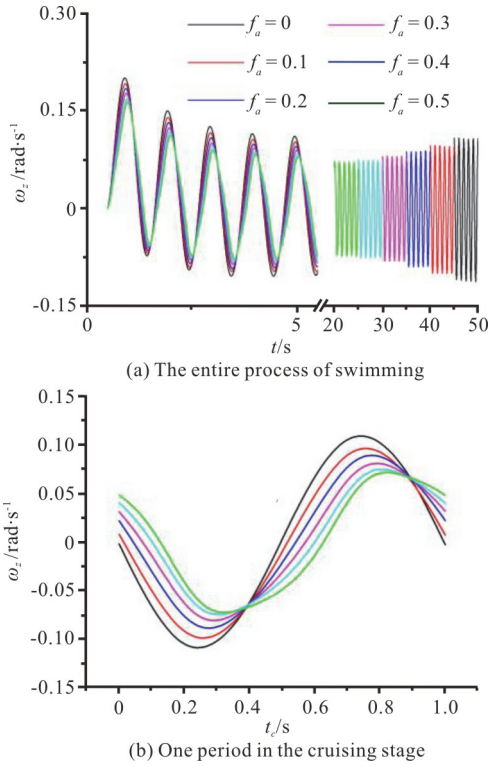

(a) The entire process of swimming

(b) One period in the cruising stage

Fig. 9 (Color online) Time history of yawing angular velocity ω_z for different f_a

explains why the swimmers with larger f_a always have smaller U_{cf} as compared with the swimmers with smaller f_a. According to Fig. 10(b), we can observe that the cycle-averaged value of F_{lrf} is always the drag-type throughout the entire swimming process. According to Fig. 10(c), we can observe that the cycle-averaged value of F_{lfr} gradually changes from the drag type to the thrust type and tends to be stable at the cruising state. According to Fig. 10(d), it can be observed that the cycle-averaged value of F_{lcf} trends to be a constant thrust-type force in the cruising state. Comparing Figs. 10(b)-10(d), it can be observed that the caudal fin provides the main thrust and the flexible rear body provides a small amount of the thrust during the entire swimming process.

The cycle-averaged value of the power consumption P_{hydro} for different f_a is shown in Fig. 11(a). The cycle-averaged value of P_{hydro} decreases until it reaches a quasi-steady state for all cases. During the cruising state, the cycle-averaged value of P_{hydro} decreases firstly as f_a is raised from 0 to 0.5 with a turning point at 0.3 and then increases as f_a is

further increased. This indicates that the flexible deformation of the caudal fin can have a benefit contribution to the decrease of the power consumption in the cruising state.

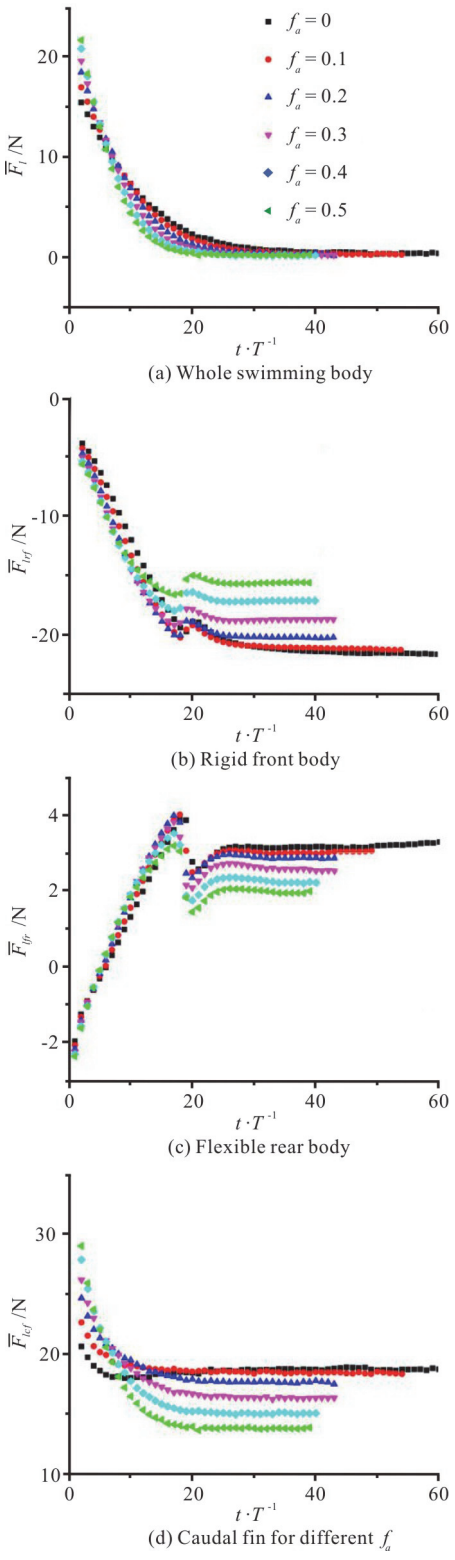

Fig. 10 (Color online) Cycle-averaged value of the longitudinal net force

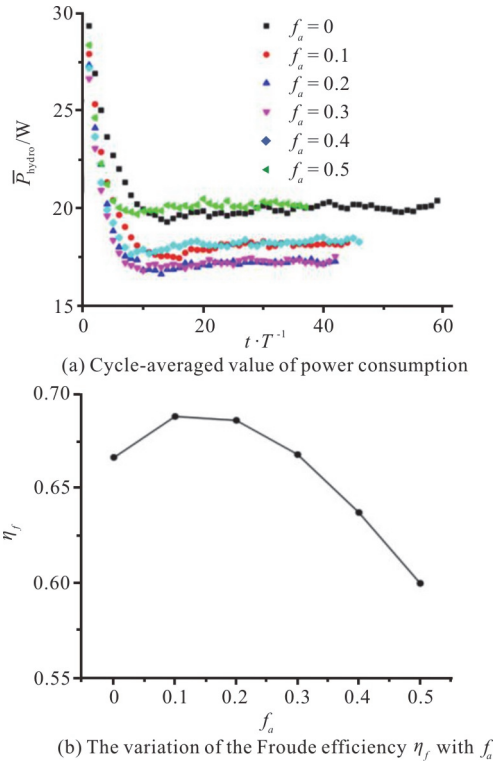

Fig. 11 (Color online) Power and efficiency

Due to the standard deviation of the Froude efficiency η_f takes a value of an order of 10^{-3} to 10^{-4} in all cases, which is a small quantity of higher order relative to the average value of η_f. Therefore, we only show the average values of η_f in Fig. 11(b), and the average values are calculated based on the last five swimming cycles. It can be observed that η_f increases firstly as f_a is changed from 0 to 0.5 with a turning point at 0.1 and then decreases as f_a is further increased. The above feature of η_f indicates that the flexible deformation of the caudal fin can have a beneficial contribution to improve the propulsive efficiency of the swimmer during the cruising state.

2.4 *Contribution of the leading-edge vortex to thrust*

As discussed in the previous sections, the caudal fin is the main propulsive part and generates the most of the thrust for the swimmer to swim forward. In this section, we investigate the mechanisms of the effect of the caudal fin deformation on the swimming performance by analyzing the vortex structures along with the pressure contours on the swimmer surface as well as the hydrodynamic forces of the caudal fin. The time histories of the longitudinal net force and the

lateral force of the caudal fin in one swimming period during cruising in all cases are shown in Fig. 12. An interesting observation in Fig. 12(a) is that F_{lcf} becomes the drag-type at two intervals during the swimming period as f_a increases, and both the duration of each interval and the maximum resistance value increase as f_a increases. For a better comparative analysis, we only consider the cases of $f_a = 0$ and $f_a = 0.5$. The vortex structures of the two cases in one swimming period in the cruising state are visualized in terms of iso-surfaces of q - criteria[25] as depicted in Figs. 13, 14. In the same figures, we also visualize the pressure contours on the swimmer surface to relate the thrust production in rigid and flexible caudal fins to the behavior of the LEVs.

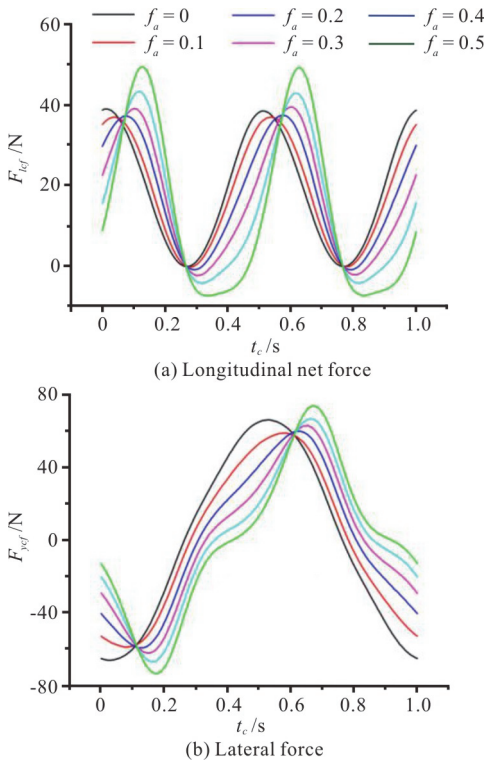

Fig. 12 (Color online) Time history of the hydrodynamic forces of the caudal fin in one cycle in the cruising stage

In the case of $f_a = 0$, at the beginning of the cycle (Fig. 13(a)) there are two fully developed LEV tubes (denoted by the vortex V-A in the left column of Fig. 13(a)) attached to the left side surface of the caudal fin, with the whole left side surface of the caudal fin covered by a low pressure region(denoted by $L_{V\text{-}A}$ in the middle column of Fig. 13(a)), and the low pressure is the largest at this instant in the cycle. At this moment, the whole right side surface of the caudal fin is covered by a high pressure region (denoted by H_1 in the right column of Fig. 13(a)), and the high pressure is the largest at this instant in the cycle. The pressure difference on two sides of the caudal fin contributes to the thrust, this contribution is the largest because the pitch angle of the caudal fin is the largest at this moment. Therefore, the longitudinal net force of the caudal fin reaches a peak value as shown in Fig. 12(a). Due to the pressure difference on two sides of the caudal fin is the largest at this moment, the lateral force of the caudal fin also reaches a peak value as shown in Fig. 12(b).

In the case of $f_a = 0.5$, at the beginning of the cycle (Fig. 14(a)) two LEV tubes (denoted by the vortex V-A in the left column of Fig. 14(a)) start to form on the left side surface of the caudal fin. In contrast to the case of $f_a = 0$, the vortex V-A is small and only attaches to the leading-edge region of the caudal fin, with a small low-pressure region in front of the caudal fin (denoted by $L_{V\text{-}A1}$ in the middle column of Fig. 14(a)). In addition, the right side of the caudal fin also has a small high-pressure region (denoted by H_1 in the right column of Fig. 14(a)). With the pressure difference on two sides of the caudal fin and the pitch angle of the caudal fin, the longitudinal net force of the caudal fin is in the thrust direction at this moment. However, due to this pressure difference is smaller, the longitudinal net force and the lateral force of the caudal fin are smaller than those in the case of $f_a = 0$ (Fig. 12).

At the point of one-quarter cycle in the case of $f_a = 0$ (Fig. 13(b)), the size of the vortex V-A is larger but with a weaker strength relative to those at the beginning of the cycle, and the V-A is shed into the wake. At this moment, there are no obvious low- and high-pressure regions on two sides of the caudal fin. The pitch angle of the caudal fin is equal to zero at this time instant, therefore, the pressure difference on two sides of the caudal fin does not contribute to the thrust. Consequently, the longitudinal net force and the lateral force of the caudal fin are close to zero (Fig. 12).

At the point of one-quarter cycle in the case of $f_a = 0.5$ (Fig. 14(b)), the size of the vortex V-A is larger relative to that at the beginning of the cycle and the whole left side of the caudal fin is covered by the vortex V-A. In contrast to the case of $f_a = 0$, the strength of the vortex V-A is larger at two tips of the caudal fin, and the vortex V-A still attaches to the two tips of the caudal fin. Consequently, there are two low-pressure regions (denoted by $L_{V\text{-}A2}$ in the middle column of Fig. 14(b)) in the left two tips of the caudal fin. In addition, there are two high-pressure regions in the right two tips of the caudal fin. Because the pitch of the caudal fin is equal to zero, the pressure difference on two sides of the caudal fin does not

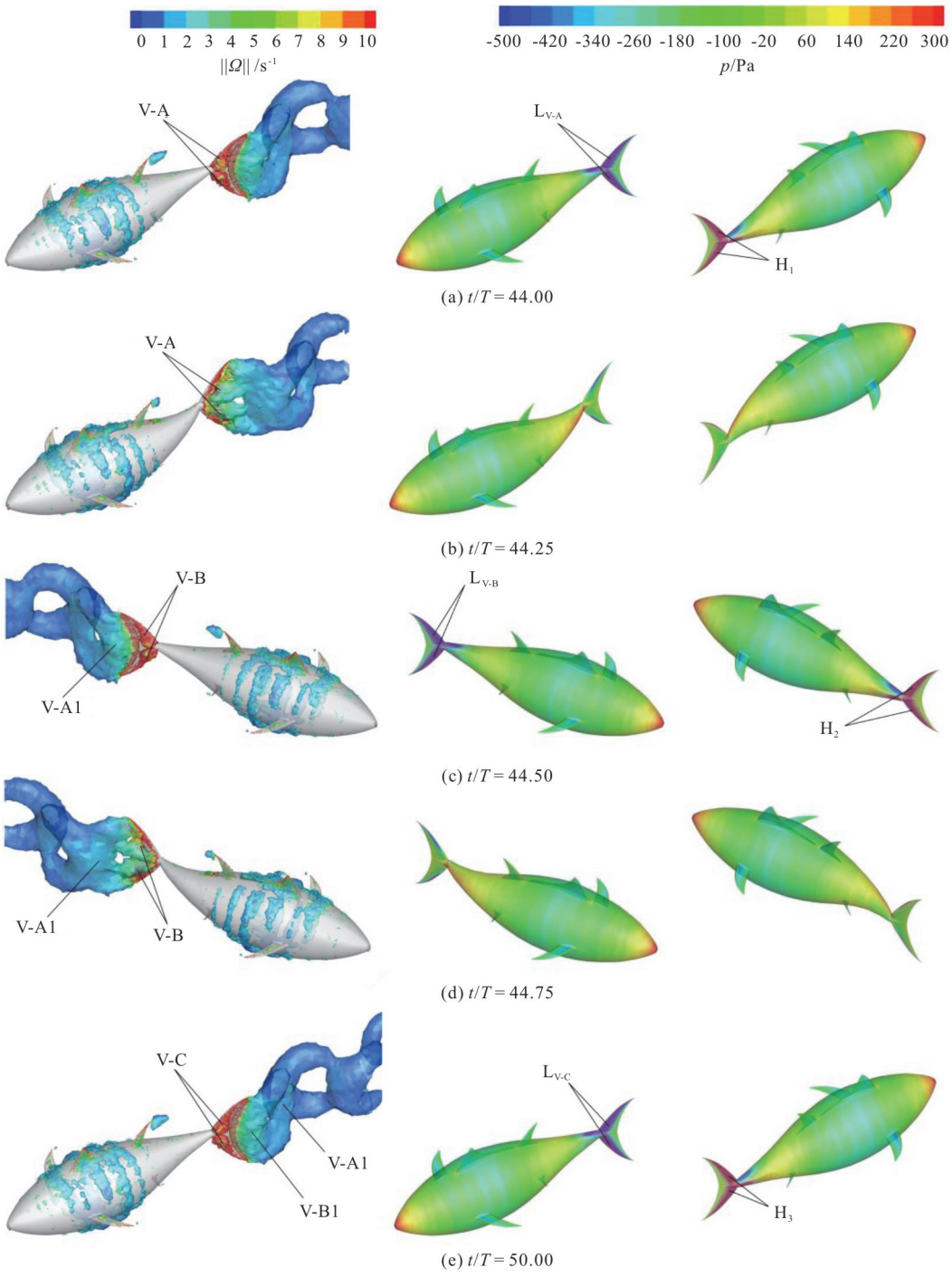

Fig. 13 (Color online) 3-D vortex structures visualized with the iso-surfaces of the q - criterion (left column) and the pressure contours on the swimmer surface (middle column and right column) in the case of $f_a = 0$ at different instants in the cycle

contribute to the thrust. Therefore, the longitudinal net force of the caudal fin is close to zero (Fig. 12(a)), whereas the lateral force of the caudal fin is not equal to zero (Fig. 12(b)).

The characteristics of the LEV and the pressure contours of the caudal fin at the point of the half cycle and at the end of the cycle are similar to those at the beginning of the cycle, and are not analyzed here in detail. Only a brief description of the evolution of the LEV in the wake structure is discussed. In both cases of $f_a = 0$, $f_a = 0.5$, between the points of the quarter and half cycle, the caudal fin flaps leftwards. During this time period, the vortex V-A moves downstream along with the caudal fin surface and

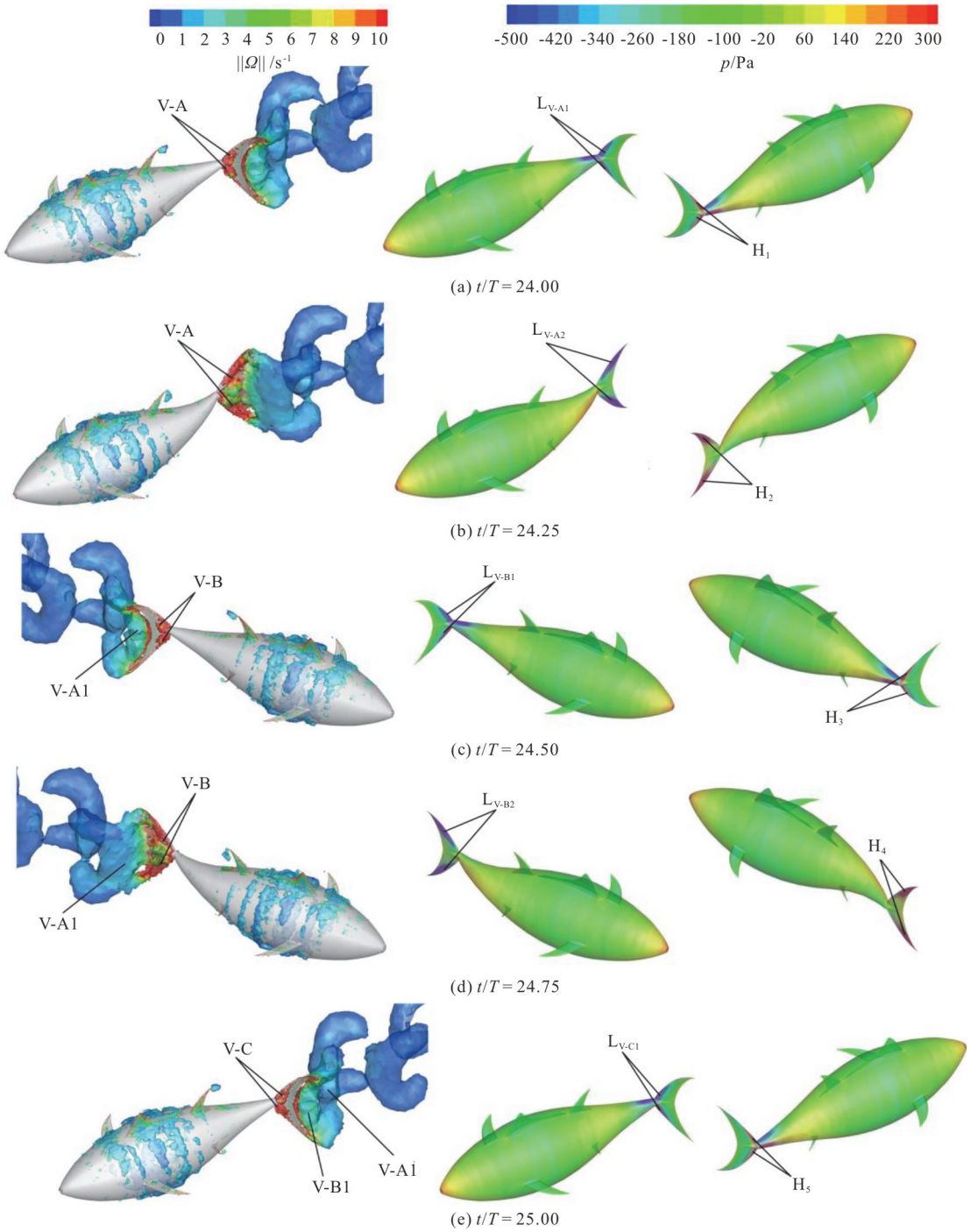

Fig. 14 (Color online) 3-D vortex structures visualized with the iso-surfaces of the q-criterion (left column) and the pressure contours on the surface of the swimmer (middle column and right column) in the case of $f_a = 0.5$ at different instants in the cycle

eventually merges with the vortex generated by the trailing edge of the caudal fin to form a big TEV (denoted by vortex V-A1 in the left column of Figs. 13(c), 14(c)). In addition, there is a new LEV (denoted by vortex V-B in the left column of Figs. 13(c), 14(c)) formed at the leading edge of the caudal fin. As the caudal fin continues its motion in the left direction, the vortex V-A1 is seen to deform along with the trailing edge of the caudal fin and is eventually shed from the trailing edge of the caudal fin at the point of three-quarter cycle (the left column of Figs. 13(d), 14(d)), with the flapping direction of the caudal fin reversed. At the end of the cycle (Figs. 13(e), 14(e)), we can observe the vortex V-A1 is separated from the

caudal fin and moves downstream, the vortex V-B merges with the vortex produced by the trailing edge of the caudal fin and a big TEV is formed (denoted by vortex V-B1 in the left column of Figs. 13(e), 14(e)), with a new LEV (denoted by vortex V-C in the left column of Figs. 13(e), 14(e)) formed at the leading edge of the caudal fin. Finally, comparing the pressure contours on the surface of the swimmer, it should be noted that the most of the thrust is produced by the leading-edge region of the caudal fin due to the contribution of the LEV.

It should be noted that the time for the longitudinal net force and the lateral force of the caudal fin to reach the peak and valley values delays with the increase of f_a (Fig. 12). To investigate the mechanism of this phenomenon, we plot the vortex structures along with the pressure contours on the surface of the swimmer at instants corresponding to the peak and the valley of the longitudinal net force of the caudal fin in the case of $f_a = 0.5$, as shown in Fig. 15. As shown in Fig. 15(a), in contrast to the case at the beginning of the cycle, the whole left side of the caudal fin is covered by the vortex V-A, leading to a larger low-pressure region in the left side of the caudal fin, and at the same time, the right side surface of the caudal fin is covered by a larger high-pressure region. Apparently, the pressure difference on two sides of the caudal fin at this instant is larger than that of the caudal fin at the beginning of the cycle. The angle that the caudal fin makes with the swimming direction (denoted by θ) is shown in the inset in Fig. 15(a), this angle makes the components of the force acting on the caudal fin larger both in the swimming and lateral directions. Consequently, both the longitudinal net force and the lateral force of the caudal fin reach the peak values at this instant (Fig. 12). As shown in Fig. 15(b), similar to the case at one-quarter cycle, the vortex V-A is still attached to the two tips of the caudal fin, leading to a low-pressure region $L_{V\text{-}A2}$ on the left side of the back half of the caudal fin, which contributes to the drag. In contrast to the case at one-quarter cycle, the vortex V-B starts to be formed on the right side of the leading edge of the caudal fin, to generate a low-pressure region $L_{V\text{-}B1}$ on the right side of the front half of the caudal fin, which contributes to the thrust. Comparing $L_{V\text{-}A2}$ and $L_{V\text{-}B1}$ in the middle and right columns of Fig. 15(b), it can be observed that the drag generated by $L_{V\text{-}A2}$ is larger than the thrust generated by $L_{V\text{-}B1}$. Therefore, the longitudinal net force of the caudal fin is in the negative swimming direction. Considering the angle that the caudal fin makes with the swimming direction (denoted by θ), the lateral force of the caudal fin is small in the left direction of the swimmer. Finally, comparing the vortex dynamics generated by the caudal fin, it should be noted that the flexible deformation of the caudal fin can lengthen the duration of the attachment of the LEV on the caudal fin.

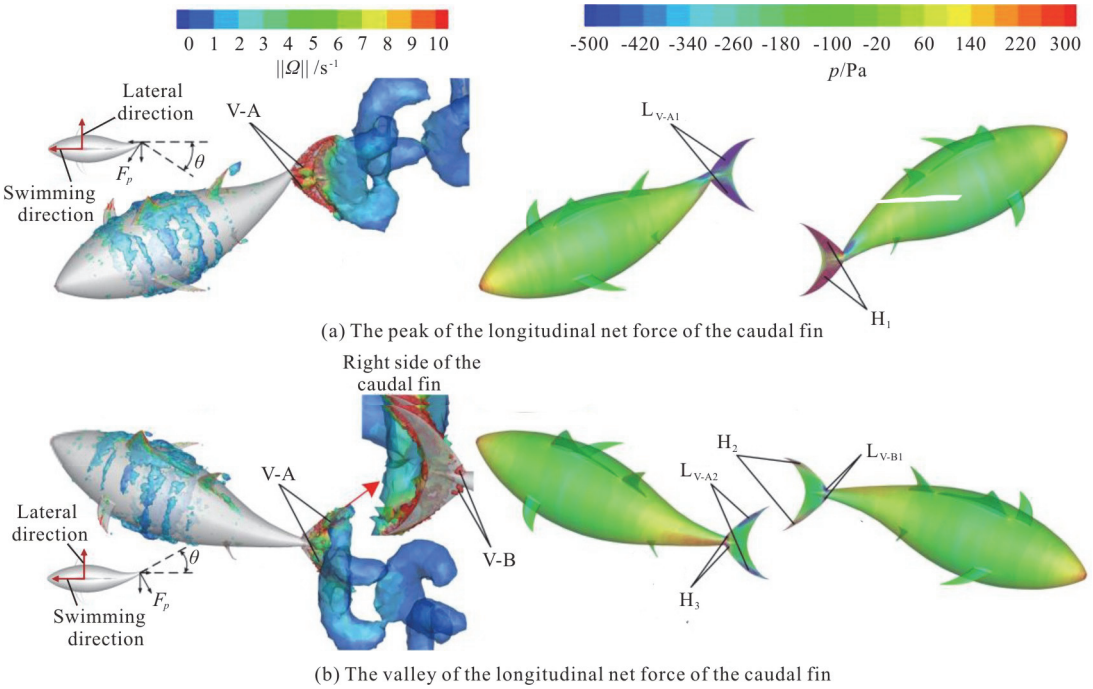

Fig. 15 (Color online) 3-D vortex structures visualized with the iso-surfaces of the q-criterion (left column) and the pressure contours on the surface of the swimmer (middle column and right column) in the case of $f_a = 0.5$

3. Conclusions

In this study, numerical simulations are carried out for the effects of the caudal fin deformation on the hydrodynamics of a self-propelled thunniform swimmer. The complex interaction of the swimmer with the fluid is analyzed by an in-house UDF program linked to the main code of the commercial flow solver FLUENT based on the fluid-body interaction method.

Our results show that the starting acceleration of the swimmer increases with the increase of the flexure amplitude f_a of the caudal fin, indicating that the caudal fin deformation can provide a larger burst force for the swimmer to begin swimming, and this burst force becomes larger with the increase of f_a. On the contrary, U_{cf} decreases with the increase of f_a. Therefore, the flexible deformation of the caudal fin contributes to the rapid start of the swimmer, but is not conducive to the high-speed cruising of the swimmer. The fluctuations of U_{cy} and ω_z during the entire swimming process decrease with the increase of f_a, that is, the caudal fin deformation is beneficial to the forward direction stability of the swimmer.

By analyzing the hydrodynamic forces of different parts of the swimmer, it is found that the caudal fin is the main propulsive part of the swimmer and that the remaining moving part of the swimmer's body can also produce a thrust, but its contribution is smaller than that of the caudal fin. During the starting stage, the cycle-averaged value of F_{lcf} monotonically increases with the increase of f_a. However, during the cruising stage, the cycle-averaged value of F_{lcf} monotonically decreases with the increase of f_a. The swimming efficiency of the swimmer with different f_a is evaluated using the Froude propulsive efficiency, the results show that the flexible deformation of the caudal fin can have a beneficial contribution to improve the propulsive efficiency in the cruising state.

Detailed analyses of the pressure field and the vortex dynamics indicate that the formation and the attachment of the LEV on the caudal fin are responsible for the generation of the thrust. The pressure contours on the swimmer surface show that the most of the thrust is produced by the leading-edge region of the caudal fin due to the attachment of the LEV. In addition, comparing the vortex structures generated by caudal fins with different f_a, it is found that the caudal fin deformation can delay the shedding of the LEV from the caudal fin and extend the duration of the low pressure on the caudal fin. During the cruising stage, the delayed shedding of the LEV makes the caudal fin generate a drag-type force over a period in one swimming period, which reduces the cruising speed of the swimmer.

References

[1] Webb P. W., Blake R. W. Swimming in functional vertebrate morphology [M]. Cambridge, USA: Harvard Univeristy Press, 1985.

[2] Webb P. W. Hydrodynamics and energetics of fish propulsion [J]. *Bulletin Fisheries Research Boad of Canada*, 1975, 190: 33-48.

[3] Videler J. J. Fish swimming [M]. London, UK: Chapman and Hall, 1993.

[4] Yang, L., Su Y. M. CFD simulation of flow features and vorticity structures in tuna-like swimming [J]. *China Ocean Engineering*, 2011, 25(1): 73-82.

[5] Tytell E. D., Lauder G. V. The hydrodynamics of eel swimming I. Wake structure [J]. *Journal of Experimental Biology*, 2004, 207: 1825-1841.

[6] Ghommem M., Bourantas G., Wittek A. et al. Hydrodynamic modeling and performance analysis of bio-inspired swimming [J]. *Ocean Engineering*, 2020, 197: 106897.

[7] Tytell E. D. Do trout swim better than eels? Challenges for estimating performance based on the wake of self-propelled bodies [J]. *Experiments in Fluids*, 2007, 43: 701-712.

[8] Borazjani I., Sotiropoulos F. Numerical investigation of the hydrodynamics of carangiform swimming in the transitional and inertial flow regimes [J]. *Journal of Experimental Biology*, 2008, 211: 1541-1558.

[9] Liu G., Ren Y., Dong H. et al. Computational analysis of vortex dynamics and performance enhancement due to body-fin and fin-fin interactions in fish-like locomotion [J]. *Journal of Fluid Mechanics*, 2017, 829: 65-88.

[10] Borazjani I., Daghooghi M. The fish tail motion forms an attached leading edge vortex [J]. *Proceedings of the Royal Society B: Biological Sciences*, 2013, 280(1756): 20122071.

[11] Kern S., Koumoutsakos P. Simulations of optimized anguilliform swimming [J]. *Journal of Experimental Biology*, 2006, 209: 4841-4857.

[12] Li G., Muller U., van Leeuwen J. L. et al. Body dynamics and hydrodynamics of swimming fish larvae: a computational study [J]. *Journal of Experimental Biology*, 2012, 215: 4015-4033.

[13] Feng Y. K., Liu H. X., Su Y. Y. et al. Numerical study on the hydrodynamics of C-turn maneuvering of a tuna-like fish body under self-propulsion [J]. *Journal of Fluids and Structures*, 2020, 94: 102954.

[14] Feng Y. K., Su Y. Y., Liu H. X. et al. Numerical simulation of a self-propelled fish-like swimmer with rigid and flexible caudal fins [J]. *Journal of Environmental Biology*, 2020, 41(2): 161-170.

[15] Cheng W. Research on simulation and control technology for bionic underwater vehicle [D]. Doctoral Thesis, Harbin, China: Harbin Engineering University, 2004(in Chinese).

[16] Dewar H., Graham J. Studies of tropical tuna swimming performance in a large water tunnel-kinematics [J]. *Journal of Experimental Biology*, 1994, 192: 45-59.

[17] Zhang X. Hydrodynamic study on biomimetic fish flipping caudal fin propulsion system [D]. Doctoral Thesis, Harbin, China: Harbin Engineering University, 2012(in Chinese).

[18] Yang L., Su Y. M., Xiao Q. Numerical study of propulsion mechanism for oscillating rigid and flexible tuna-tails [J]. *Journal of Bionic Engineering*, 2011, 8(4): 406-417.
[19] Li N., Liu H., Su Y. Numerical study on the hydrodynamics of thunniform bio-inspired swimming under self-propulsion [J]. *Plos One*, 2017, 12(3): e0174740.
[20] Hu J., Xiao Q. Three-dimensional effects on the translational locomotion of a passive heaving wing [J]. *Journal of Fluids and Structures*, 2014, 46: 77-88.
[21] ANSYS Inc. ANSYS Fluent User's Guide [R]. ANSYS Inc., 2015.
[22] Bergmann M., Lollo A., Mittal R. Effect of caudal fin deformation on the propulsive efficiency of a fish-like swimmer [J]. *Bioinspiration and Biomimetics*, 2014, 9(4): 046001.
[23] Leroyer A., Visonneau M. Numerical methods for RANSE simulations of a self-propelled fish-like body [J]. *Journal of Fluids and Structures*, 2005, 20: 975-991.
[24] Donley J. M., Dickson K. A. Swimming kinematics of juvenile kawakawa tuna (*Euthynnus affinis*) and chub mackerel (*Scomber japonicus*) [J]. *Journal of Experimental Biology*, 2000, 203: 3103-3116.
[25] Hunt J. C. R., Wray A. A., Moin P. Eddies, streams, and convergence zones in turbulent flows [R]. Proceedings of the Summer Program. Center for Turbulent Research Report CTR-S88,1988, 193-208.